Applied Physics Letters ARTICLE pubs.aip.org/aip/apl

# Enhancement of spin Seebeck effect in $Fe_3O_4$/Pt thin films with α-Fe nanodroplets

Cite as: Appl. Phys. Lett. **123**, 172408 (2023); doi: 10.1063/5.0165851
Submitted: 30 June 2023 · Accepted: 9 October 2023 ·
Published Online: 27 October 2023



G. Venkat,[1,2] C. D. W. Cox,[1] Z. Zhou,[3] N. Leo,[4] C. J. Kinane,[5] A. J. Caruana,[5] and K. Morrison[1,a)]

## AFFILIATIONS

[1]Department of Physics, Loughborough University, Loughborough LE11 3TU, United Kingdom
[2]Department of Materials Science and Engineering, University of Sheffield, Sheffield S1 3JD, United Kingdom
[3]Loughborough Materials Characterisation Centre, Loughborough University, Loughborough LE11 3TU, United Kingdom
[4]Instituto de Nanociencia y Materiales de Aragón (INMA), CSIC–Universidad de Zaragoza, 50009 Zaragoza, Spain
[5]ISIS Neutron and Muon Source, Didcot, Oxfordshire OX11 0QX, United Kingdom

**Note:** This paper is part of the APL Special Collection on Ferrimagnetic Spintronics.
[a)]**Author to whom correspondence should be addressed:** k.morrison@lboro.ac.uk

## ABSTRACT

In this study, we demonstrate an enhancement of the measured spin Seebeck coefficient in $Fe_3O_4$/Pt bilayer films due to an increase in Fe nanodroplets formed by pulsed laser deposition. Four bilayer films were deposited at the same time from a highly textured target, resulting in a general increase in droplet formation that was confirmed to be Fe rich by scanning electron microscope and transmission electron microscope-dispersive x-ray spectroscopy. Of these four films, there were two distinct groupings with differing density of α-Fe droplets, where the bilayer with higher droplet density exhibited a 64% increase in the measured spin Seebeck coefficient from 38 to 63 nV m/W.





The spin Seebeck effect (SSE), first observed in 2008,[1] is defined by spin accumulation in a magnetic material as a result of a temperature gradient and has been observed in a wide variety of materials, notably yttrium iron garnet (YIG) as an insulator with low damping as well as magnetite ($Fe_3O_4$), a ferrimagnetic semiconductor at room temperature that becomes insulating below the Verwey transition at 120 K.[2] The possible applications of the spin Seebeck and other magnetothermal effects (such as the anomalous Nernst effect, ANE) include their use in heat flux sensors,[3] thermoelectrics,[4,5] and as a spin current source in spintronics devices. However, for spin Seebeck devices, we require utilization of this spin accumulation by spin pumping into an adjacent paramagnetic layer, such as Pt, where it is converted to a measurable voltage via the inverse spin Hall effect (ISHE).[6] As such, the efficiency of this spin injection has a significant role to play in the application of any spin Seebeck based devices.

There have been several studies that have demonstrated that the nature of the interface between magnetic and paramagnetic layers has an impact on the efficiency of spin injection into the paramagnetic layer.[7–12] For example, for YIG/Pt bilayers, a strong dependence of the spin pumping efficiency was observed with YIG surface treatment prior to Pt deposition (with spin mixing conductance, $g_r$, varying from $0.02 \times 10^{19}$ to $3.43 \times 10^{19}$ $m^{-2}$).[7] With regard to interfacial roughness, there are conflicting reports of improvement in spin injection: e.g., a linearly increasing relationship between $g_r$ and roughness of $Fe_3O_4$/Pt bilayers,[12] or an order of magnitude decrease in ISHE measured in YIG/Pt bilayers with increasing roughness.[8] As a separate route to improve spin injection, the insertion of ultrathin magnetic layers of NiO, Mn, IrMn, or Ru was shown to enhance the measured spin Seebeck voltage of YIG/Pt bilayers by up to 100%; however, this was partly due to the modification of the resistance.[10] Theoretically, first principle calculations modeling the different types of disorder at a Permalloy/platinum interface have indicated that introducing a foreign magnetic metal layer into the Pt could result in an increase in the spin injection efficiency,[13] or that a surface-roughness-induced increase in the spin Hall effect (thus increased efficiency of spin current conversion to charge current) could occur due to side jump scattering.[14] In this Letter, we will show an enhancement of the spin Seebeck coefficient measured for $Fe_3O_4$/Pt bilayers with the inclusion of α-Fe nanodroplets.

$Fe_3O_4$/Pt thin films with nominal thicknesses of 80/5 nm were deposited simultaneously onto four 10 × 10 $mm^2$ borosilicate glass substrates by pulsed laser deposition (PLD). Deposition occurred

under UHV conditions ($<10^{-9}$ mbar) from a polycrystalline $Fe_2O_3$ target (Pi-kem, purity 99.9%), with $\lambda = 532$ nm, a pulse width of 8 ns, and a 10 Hz repetition rate. We have shown previously that 80 nm thick $Fe_3O_4$ films grown by PLD in this way are typically preferentially textured out of plane ⟨111⟩, with a grain size equivalent to the film thickness (80 nm), suggesting columnar growth.[15] In this work, however, we report on films produced from heavily textured/ablated targets that resulted in an increase in droplet formation.[16,17] Note that the substrate carrier was not rotated during deposition, which results in the small variations in the film deposition observed here.

Structural characterization was carried out using a combination of x-ray diffraction (XRD) on a Bruker D2 phaser and x-ray reflectivity (XRR) on a Siemens D5000. In addition, polarized neutron reflectometry (PNR) measurements were performed on the PolRef (ISIS, UK) beamline, with the OSMOND 1D detector,[18] and fit using the Refl1D software package.[19]

The microstructure and chemical distribution of the thin film layers were examined using a FEI Tecnai F20 field emission gun scanning transmission electron microscope (FEGSTEM). Images of the cross sections of the layers were recorded in scanning mode with a probe size of ~1 nm using the high angle annular dark field (DF) (HAADF, Fischione) and bright field (BF, Gatan) detectors. The TEM was also equipped with an Oxford Instruments X-MaxN 80 TLE windowless x-ray detector to allow energy dispersive x-ray spectroscopy (EDS) for chemical mapping. Cross sections of thin films for STEM were prepared using a FEI Nova 600 nanoLab focused ion beam (FIB)/scanning electron microscope (SEM).[15,20] The TEM lamella had a thickness of approximately $100 \pm 20$ nm for EDS measurements and 30 nm for high resolution imaging.

Sheet resistance measurements of the bilayers were obtained using the van der Pauw geometry. Finally, spin Seebeck measurements were obtained using the heat flux method at room temperature.[21,22] All samples were the same geometry ($8 \times 8\,mm^2$ active area) and mounted similarly; further details can be found elsewhere.[15,21,27]

Figure 1 shows a schematic of the substrate orientation with respect to the target and laser direction during deposition, and XRD for the four films that were deposited (labeled G50#1–#4). Initial analysis of the XRD patterns only indicated subtle differences between the four samples: (1) minor differences in the height and full width maximum of the Pt (111) peak at $2\theta = 39.65°$; (2) changes in the height of the Bragg peak at $2\theta = 44.7°$, which we attribute to an α-Fe phase; and (3) emergence of a minor feature at $2\theta = 42.4°$ for samples G50#2 and G50#4. The difference in the Pt (111) peak is likely due to a combination of slightly different Pt thicknesses and strain or disorder. Corresponding analysis of XRR confirmed that the Pt thicknesses, $t_{Pt}$, differed slightly between samples, as summarized in Table I, which also manifested in variations of the measured sheet resistance of each sample, $R_s$. The resistivity, $\rho = R_s t_{Pt}$, was consistently around $2.2 \times 10^{-7}\,\Omega\,m$, as expected for these bilayers.[15]

Figure 2 shows electron microscopy measurements of G50#1 and G50#2. Top–down SEM and EDS indicated a stark difference in surface texture: whereas G50#1 had multiple plate like formations, and G50#2 had a lower density of droplets that were more well-formed; corresponding EDS indicated that these droplets were strongly Fe rich. Figures 2(c) and 2(d) show STEM/BF, and Figs. 2(e) and 2(f) show HAADF images of the typical cross sections of G50#1 and #2. The corresponding EDS maps of the $Fe_3O_4$/Pt area are also shown for Pt, Fe,

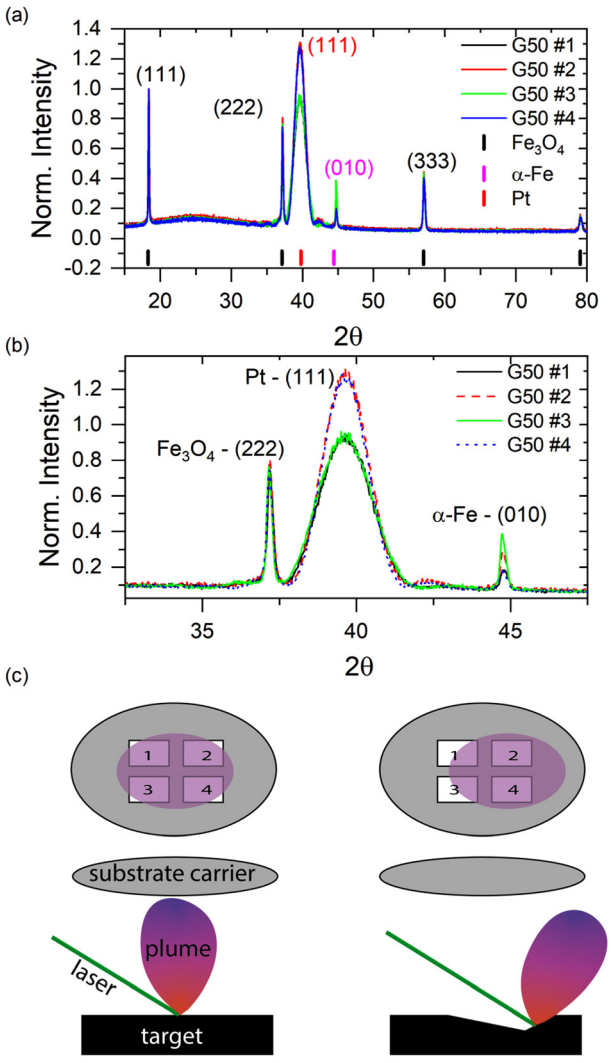


**FIG. 1.** (a) XRD of the four samples, with observed Bragg peaks due to $Fe_3O_4$, Pt, and α-Fe indicated. (b) Close-up of XRD data around the Pt reflection. (c) Geometry of the substrate carrier with respect to the laser, target, and plume. The substrate carrier is shown top–down (top) and side-on (middle), with the position of the substrates labeled as #1–4. The image on the right indicates the shift in the plume due to target texturing.

**TABLE I.** Summary of Pt thickness, $t_{Pt}$, estimated from the Pt fringe separation observed in XRR (error taken as standard deviation of this estimate where multiple fringes were observed, and 10% otherwise), sheet resistance, $R_s$, and resistivity, $\rho$.

| Sample | $t_{Pt}$ (nm) | $R_s$ (Ω/sq) | $\rho$ ($10^{-7}$ Ω m) |
|---|---|---|---|
| G50#1 | $4.7 \pm 0.1$ | 49 | $2.3 \pm 0.1$ |
| G50#2 | $5.3 \pm 0.5$ | 37 | $2.0 \pm 0.2$ |
| G50#3 | $4.5 \pm 0.2$ | 48 | $2.1 \pm 0.1$ |
| G50#4 | $5.4 \pm 0.1$ | 40 | $2.2 \pm 0.1$ |

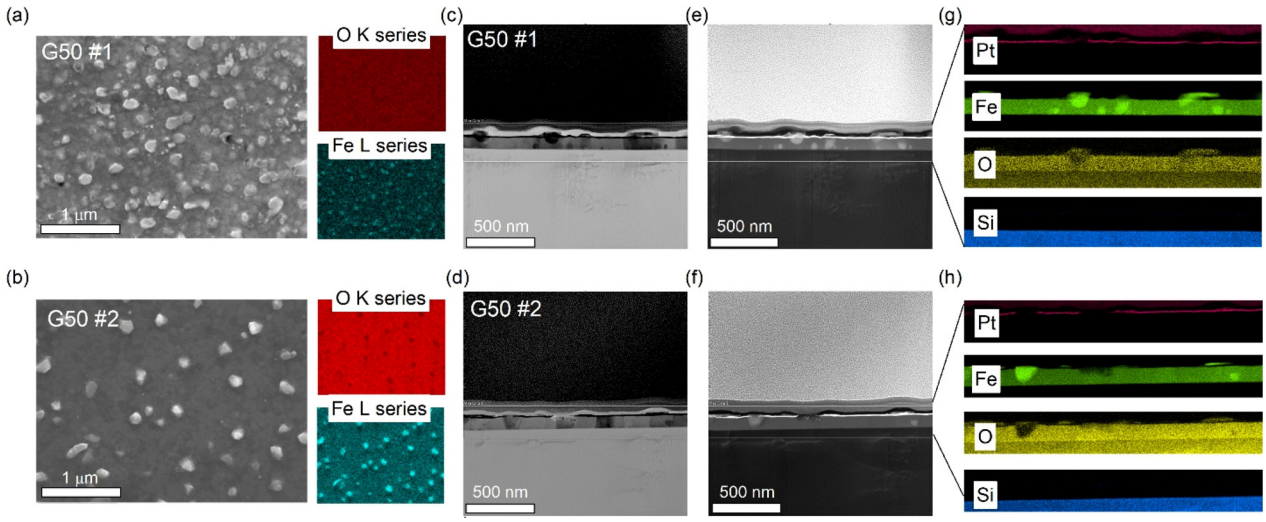


**FIG. 2.** Electron microscopy of G50#1 (top) and G50#2 (bottom). (a) and (b) Top–down scanning electron microscopy and corresponding EDS maps for Fe and O. (c) and (d) Bright field (BF) TEM. (e) and (f) Dark field (DF) TEM, and (g) and (h) corresponding EDS maps from the thin film region.

O, and Si. The BF images showed a polycrystalline magnetite layer with a thickness of approximately 85.2 ± 2.8 nm and an estimated Pt thickness of 8.7 ± 0.2 nm. The errors here come from the HRTEM lattice, but we expect that the surface waviness across the 100 nm slice resulted in differences between values estimated by XRR and TEM.

In line with the Fe maps, a number of Fe-rich, O-deficient spherical regions were present throughout the magnetite layer, varying from 30 to 80 nm in diameter, indicating that they are likely to be Fe droplets. This is in contrast to previous TEM of $Fe_3O_4$/Pt bilayers produced using the same system and method, but with a much less textured target.[15] The major difference in the two samples lies in the population density of the Fe droplets, i.e., from this small slice G50#1 appeared to have 4–5 times more Fe droplets throughout the layer than G50#2, as highlighted in the Fe (and O by loss of contrast) EDS maps.

As mentioned already, the films presented here were deposited from a $Fe_2O_3$ target that had been previously ablated sufficiently enough to cause significant texturing of the target. Electron microscopy confirmed that this results in an increase in droplet formation, which agrees with previous observations as the deposition target is degraded.[17,23,24] While it is a common practice to use a dense or freshly polished target in order to suppress droplet formation,[25] we use this feature here to explore the impact of the inclusion of α-Fe nanodroplets on measured magnetothermal effects (SSE + ANE). We argue that due to alignment of the substrates, as the target became more heavily textured, the plume was redirected so that substrates G50#1 and #3 were situated closer to the edge of the plume [see Fig. 1(c)]. It has been shown that droplets are likely to be found on the circumference zone of the laser,[26] hence the higher droplet density observed in G50#1 (Fig. 2, top panel).

Figure 3 shows representative magnetothermal measurements for these samples as well as a similar series produced from a previously textured target (G18#1–4), and a summary of the spin Seebeck coefficient obtained. Nominal thicknesses of 80 nm $Fe_3O_4$ and 5 nm Pt were

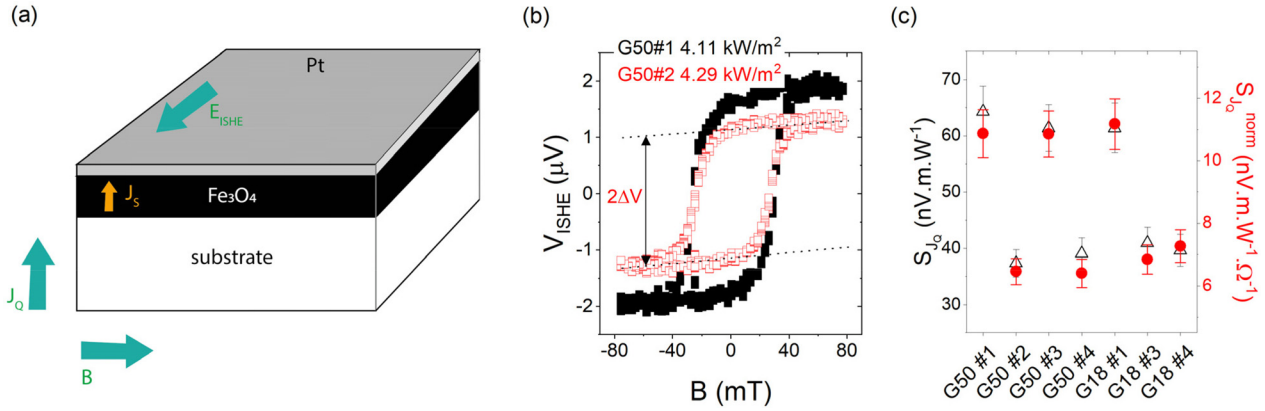


**FIG. 3.** (a) Schematic of the SSE measurement geometry. (b) Example raw data as a function of magnetic field for G50#1 and #2 at similar $J_q$. (c) Summary of spin Seebeck coefficient normalized as detailed in text, for G50 and G18 series [black open triangles—Eq. (1), and red closed circles, Eq. (3)].

chosen for reproducibility with prior work, in particular the observed saturation of the spin Seebeck signal for $t_{Fe3O4} > 80$ nm at approximately 47 nV m/W.[27] Any small differences in the $Fe_3O_4$ thickness should, therefore, not have an impact of the observed spin Seebeck signal.

Based on previous work, we argue that the ANE in the $Fe_3O_4$ (and proximity-induced ANE in the Pt) can be considered negligible compared to the spin Seebeck effect in the $Fe_3O_4$/Pt bilayers.[28] With regard to the impact of the Fe nanodroplets, prior work by Bavontaweepanya *et al.* measured the magnetothermal effect in Fe films on Si and polycrystalline bulk $Fe_3O_4$ coated with 10 nm Fe, where the ANE in Fe was shown to contribute approximately 50% of the magnetothermal voltage measured for $Fe_3O_4$/Fe.[29] However, in this case, the magnetothermal effect in the $Fe_3O_4$/Fe bilayers is an order of magnitude lower than that observed in $Fe_3O_4$/Pt, and therefore unlikely to result in the increased magnetothermal effect seen in these films. Assuming that we can consider contributions due to ANE as negligible in this case, there are several methods that are used to normalize spin Seebeck data. As we are comparing thin films, we use the heat flux method,[21,22] which is insensitive to temperature drops at interfaces and has been shown by a round robin study to be more reliable.[30] In such a case, the spin Seebeck coefficient, $S_{Jq}$, can be described by

$$S_{J_q} = \frac{V_{ISHE} A_{xy}}{Q L_y}, \tag{1}$$

where $V_{ISHE}$ is the inverse spin Hall effect voltage generated in the Pt layer due to injection of a spin current from the $Fe_3O_4$ layer, $A_{xy}$ is the cross-sectional area of the sample, Q is the heat (in watts) that passes through $A_{xy}$, and $L_y$ is the contact separation. Note that this can be converted to the spin Seebeck coefficient normalized by temperature gradient, $\nabla T$,

$$S_{\nabla T} = \frac{V_{ISHE} L_z}{\Delta T L_y}, \tag{2}$$

where $L_z$ is the thickness of the sample and $\Delta T$ is the temperature difference across it, if the thermal conductivities of the substrate and thin film layers are known.[22]

As can be seen in Fig. 3(c) (black triangles), there was a significant difference in the measured spin Seebeck coefficient, $S_{Jq}$, for our set of samples: G50#1 and #3 exhibited significantly higher $S_{Jq}$ than G50#2 and #4. It could be argued that this was due to the differences in the resistance and thicknesses of the Pt layer, so to account for this, we set a modified spin Seebeck coefficient,

$$S_{J_Q}^{norm} = \frac{S_{J_Q}}{\eta \tanh\left(\frac{t_{Pt}}{2\lambda_{Pt}}\right)\frac{\rho_{Pt}}{t_{Pt}}}, \tag{3}$$

where the denominator follows from descriptions of spin injection and conversion to $V_{ISHE}$,[31] $\lambda_{Pt}$ is the spin diffusion length of the Pt layer [taken here to be 8 nm (Ref. 32)], and $\eta$ is defined by

$$\eta = \left\{1 + 2g_r \rho_{Pt} \lambda_{Pt} \frac{e^2}{h} \coth\left(\frac{t_{Pt}}{\lambda_{Pt}}\right)\right\}^{-1}, \tag{4}$$

where $g_r$ is the spin mixing conductance [taken here to be $5 \times 10^{18}$ m$^{-2}$ (Ref. 33)], $\rho_{Pt}$ is the Pt layer resistivity (noted in Table I), $h$ is Planck's constant, and $e$ is the charge of an electron. The result of this normalization is also shown in Fig. 3 (red dots), where it is clear that the slight differences in $t_{Pt}$ for this series of samples is not the source of the enhancement of $S_{Jq}$.

To summarize, there is a clear grouping of $S_{Jq}$ for samples deposited at the same time: a subset that demonstrates $S_{Jq} \approx 38$ nV m/W, similar to previously reported values,[27] and a second subset that exhibits a 64% increase to approximately 63 nV m/W. This is a significant enhancement of the voltage generated *for films deposited at the same time*. Also shown in Fig. 3 is $S_{Jq}$ measured for another set of samples, G18. In this case, a similar trend was observed, but due to sample degradation and limited information on substrate placement with respect to the plume, we were unable to confirm that an increase in Fe droplets was the source of this enhancement. We include here only to demonstrate the reproducibility of this effect for highly textured targets.

As electron microscopy only provides a small snapshot of the films, we also used PNR to probe the depth-dependent structure and magnetization of the layers, averaged in the *xy*-plane. Data were obtained at a positive field saturation (700 mT) and in a smaller field of 14 mT after negative field saturation of −700 mT. As seen in Fig. 4, a clear splitting in the PNR up ($u$) and down ($d$) scattering cross sections was observed, which is a direct response of the magnetic scattering from the sample. There were also clear fringes that primarily arose from the $Fe_3O_4$/Pt bilayer. [We show XRR data for the for samples in Fig. 4(a) as well, to demonstrate the contrast observed due to the Pt layer.] These data were first fit using a standard "slab" bilayer model, where the interfaces were modeled using analytical error function profiles. As the neutron scattering length for $Fe_3O_4$ and Pt is closely matched, we used data from XRR and SEM to constrain the fit of the Pt layer to be within 10% of the estimates summarized in Table I. The scattering length density (SLD) profile obtained from the best fits using this model confirmed a slightly thinner $Fe_3O_4$ layer for G50#3, which is consistent with the assumption that it lays on the circumference of the plume (hence lower deposition rate and higher droplet density). However, the posterior distributions of fit parameters for thickness of the Pt layer ($t_{Pt}$) showed a strong preference to decrease down to the lower bound of the limit imposed by our model. Furthermore, the two roughness parameters ($\sigma_i$ and $\sigma_t$) show a strong correlation (Pearson correlation $p \approx 0.6$), indicating that for this model parameterization, there was not enough information in the data to uniquely determine these values.

To address the limitations of the bilayer model, we also fit the data to a modified model of the surface that enables a physically meaningful description of the Fe nanodroplets seen with SEM and TEM. We refer to this model here as the "morphological model" and provide a schematic of the key features in Fig. 5(d). For this model, we assumed that the nanodroplets were half spheres of Fe (light blue), with radius $r_0$ placed on top of the $Fe_3O_4$ layer (dark blue) and covered with a fully conformal overlayer coating (Pt) with thickness $t_{Pt}$ (gray). The parameter $f_N$ described the particle area density of non-overlapping nanodroplets with hexagonal packing. The SLD profile above $z_0 = t_{Fe_3O_4}$ could then be written as a sum of the different geometric contributions as follows:

$$SLD(z') = A_{ref}^{-1}\left[\rho_{Fe} dA(z', r_0) + f_N \rho_{Pt}[dA(z', r_0 + t_{Pt}) - dA(z', r_0)] + (1 - f_N)\rho_{Pt} dA(z', t)\Theta(t_{Pt} - z')\right], \tag{5}$$

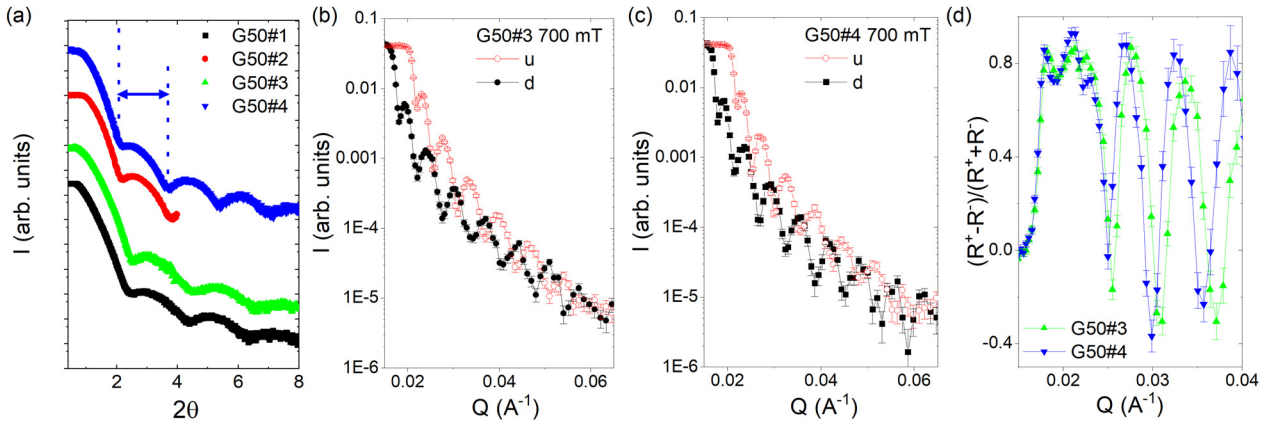


**FIG. 4.** (a) XRR for G50#1–4, where the major fringe used to estimate Pt thickness is indicated. (b) and (c) PNR for G50#3 and #4, respectively, and (d) corresponding PNR asymmetry plots at +700 mT.

where $\rho_{Fe}$ and $\rho_{Pt}$ are the scattering length densities of the Fe and Pt layers, respectively, $dA(z', r)$ is the effective SLD of a half sphere with radius $r_0$ starting at $z' = z - z_0$,

$$dA(z', r_0) = {r_0}^2 \cos^2\left(\frac{\pi z'}{2 r_0}\right)\Theta(z')\Theta(r_0 - z'), \tag{6}$$

and $A_{ref} = \frac{2\sqrt{3}(r_0+t_{Pt})^2}{f_N}$ is the reference area for one half sphere in hexagonal packing. The parameter $\Theta(x)$ denotes the error function, for which we assumed a general narrow width of 5 Å. For simplicity, we assumed no statistical spread of the structural values of $r_0$, $t_{Pt}$, or $f_N$. As this model considers two differently distributed materials with different SLDs, i.e., $\rho_{Fe}$ and $\rho_{Pt}$, it also allowed us to consider different contributions to the magnetic contrast from $Fe_3O_4$ and Fe.

The SLDs obtained using the morphological model are shown in Fig. 5(e). While we fixed the value of $\rho_{Fe}$ to that of bulk Fe, the value of $\rho_{Pt}$ was allowed to vary to consider that the Pt layer may not be continuous across the entire film. Figure 5(f) shows the posterior distributions for $r_0$, $t_{Pt}$, and the derived area particle density $n_A = \frac{f_N}{2\sqrt{3}r_0^2}$.

The mean values of $r_0$ were 45.6 ± 2.3 nm and 47.1 ± 1.7 nm for G50#3 and G50#4, respectively, which correlates well with typical particle sizes observed in SEM and TEM. Typical particle area densities, $n_A$, ranged from about 25 to 55 particles/$\mu m^2$, which again agreed with particle counts in SEM images (Fig. 2). From the magnetic SLD, $\rho_M$,

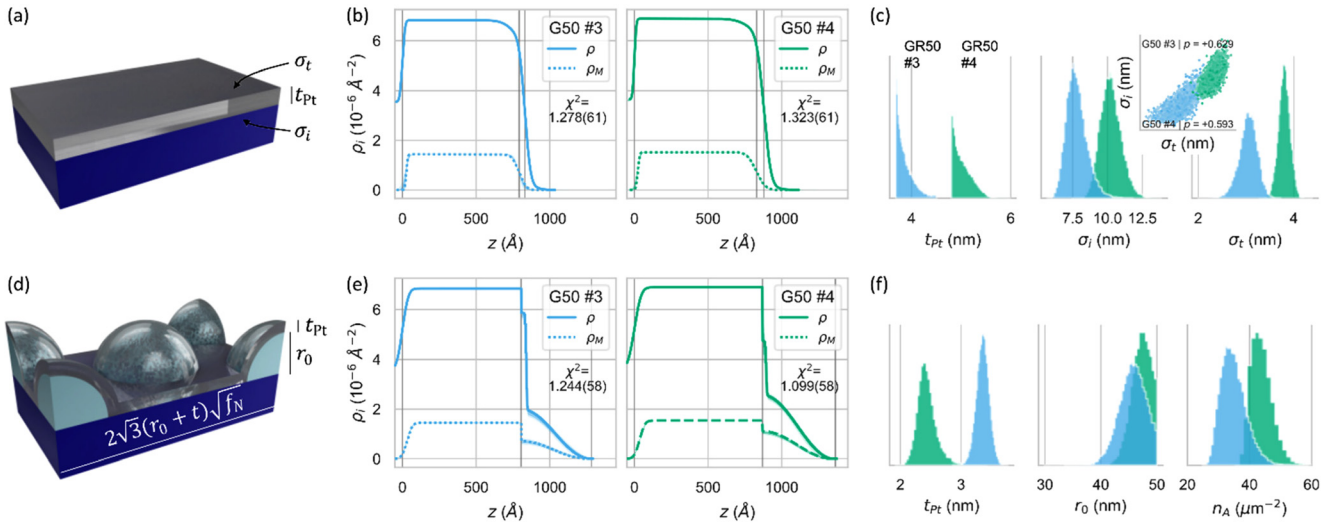


**FIG. 5.** (a) Schematic of the bilayer model used, with top layer thickness, $t_{Pt}$ (gray). Gaussian roughness at the bottom and top interfaces was described by parameters $\sigma_i$ and $\sigma_t$, respectively. (b) Representative best fit of structural (solid) and magnetic (dashed) SLDs obtained for samples G50 #3 and #4 using the bilayer model, with 68% and 95% uncertainty intervals marked. (c) Posterior distributions of fit parameters $t_{Pt}$, $\sigma_i$, and $\sigma_t$. (d) Morphological model detailed in text, where half spheres (light blue) of radius $r_0$ and particle density $f_N$ were conformally covered by a layer of thickness $t_{Pt}$ (gray). (e) Corresponding best fit SLDs. (f) Posterior distributions of fit parameters $r_0$, $t_{Pt}$, and particle area density $n_A$.

we calculated the saturation magnetization as 497 ± 19 (G50#3) and 528 ± 16 kA/m (G50#4) for the $Fe_3O_4$ film, similar to previously measured moment of 465 kA/m.[15] For the Fe droplets, we found 1110 ± 11 (G50#3) and 1190 ± 65 kA/m (G50#4), which is lower than the bulk saturation magnetization of 1700 kA/m, but not unexpected for α-Fe nanoparticles. The values of $t_{Pt}$ were less than suggested from XRR and HRTEM, which is likely due to thickness variations in the flat and curved areas of the film that were not accounted for with our model. Regardless of the simplified assumptions, the morphological model allowed us to extract general parameters describing the surface morphology.

To summarize, a series of $Fe_3O_4$/Pt thin films were prepared with varying density of Fe nanodroplets. It was shown that for the samples with higher density of these nanodroplets, there was a 64% increase in the observed magnetothermal voltage, which far exceeds any expected change due to additional ANE in the Fe nanodroplets. We showed using PNR that there was no significant change in the magnetization of the $Fe_3O_4$ layer, and that the Fe nanodroplets could also be contributing some magnetic moment to the device. As the contribution due to ANE in the $Fe_3O_4$, Pt layers, and Fe nanodroplets can be considered negligible in this case, and PNR does not show a significant difference in magnetization at the interface, we suggest that the observed enhancement of the SSE is due to a combination of modification of the interface roughness and impact of the Pt coated Fe nanodroplets on spin injection efficiency. Previous observations of an increase in spin mixing conductance in $Fe_3O_4$/Pt layers with interface roughness would suggest an upper limit increase of 20% (based on the RMS roughness doubling).[12] While possible ANE contributions from the Fe nanodroplets are expected to be negligible due to the low volume content and comparatively lower signal,[29] they could result in local magnetization of the Pt layer that would enhance any proximity induced ANE. In addition, we argue that the inclusion of Fe in the Pt may have resulted in an increase in spin injection efficiency as theorized by Zhang *et al.*[13] This relationship between the surface morphology and spin caloritronic effects suggests a route to engineer the efficiency of spin Seebeck-based devices, e.g., for waste heat recovery, and determining the exact nature of this increase will be the focus of future work.

The authors acknowledge Dr. Keith Yendall, Mr. Sam Davis, and the Loughborough Materials Characterisation Centre for assistance and use of the facilities. This work was supported by the Engineering and Physical Sciences Research Council (No. EP/P006221/1). N.L. received funding from the European Research Council (ERC) under European Union's Horizon 2020 Program, Contract No. 101001290 (3DNANOMAG).

## AUTHOR DECLARATIONS

### Conflict of Interest

The authors have no conflicts to disclose.

### Author Contributions

**Guru Venkat:** Formal analysis (equal); Writing – original draft (supporting); Writing – review & editing (equal). **Christopher Cox:** Formal analysis (equal); Resources (equal); Writing – original draft (supporting); Writing – review & editing (equal). **Zhaoxia Zhou:** Formal analysis (equal); Writing – original draft (supporting); Writing – review & editing (equal). **Naëmi Leo:** Formal analysis (equal). **Christy J. Kinane:** Formal analysis (equal); Methodology (equal). **Andrew Caruana:** Formal analysis (equal); Writing – original draft (supporting); Writing – review & editing (equal). **Kelly Morrison:** Formal analysis (equal); Funding acquisition (lead); Methodology (equal); Supervision (equal); Writing – original draft (lead); Writing – review & editing (equal).

## DATA AVAILABILITY

The data that support the findings of this study are openly available in PolRef at https://doi.org/10.5286/ISIS.E.RB2010586-1, Ref. 34 and Loughborough at https://doi.org/10.17028/rd.lboro.6383984, Ref. 35.

## REFERENCES

[1]K. Uchida, S. Takahashi, K. Harii, J. Ieda, W. Koshibae, K. Ando, S. Maekawa, and E. Saitoh, Nature **455**, 778–781 (2008).
[2]K. Uchida, M. Ishida, T. Kikkawa, A. Kirihara, T. Murakami, and E. Saitoh, J. Phys.: Condens. Matter **26**, 343202 (2014).
[3]A. Kirihara, K. Kondo, M. Ishida, K. Ihara, Y. Iwasaki, H. Someya, A. Matsuba, K. Uchida, E. Saitoh, N. Yamamoto, S. Kohmoto, and T. Murakami, Sci. Rep. **6**, 23114 (2016).
[4]Y. Kurokawa, Y. Tahara, Y. Hamada, M. Fujimoto, and H. Yuasa, Sci. Rep. **12**, 16605 (2022).
[5]M. Y. Kim, S. J. Park, G.-Y. Kim, S.-Y. Choi, and H. Jin, Energy Environ. Sci. **14**, 3480–3491 (2021).
[6]J. E. Hirsch, Phys. Rev. Lett. **83**, 1834 (1999).
[7]M. B. Jungfleisch, V. Lauer, R. Neb, A. V. Chumak, and B. Hillebrands, Appl. Phys. Lett. **103**, 022411 (2013).
[8]A. Aqeel, I. J. Vera-Marun, B. J. van Wees, and T. T. M. Palstra, J. Appl. Phys. **116**, 153705 (2014).
[9]Z. Qiu, D. Hou, K. Uchida, and E. Saitoh, J. Phys. D **48**, 164013 (2015).
[10]F. Nakata, T. Nimura, Y. Kurokawa, and H. Yuasa, Jpn. J. Appl. Phys., Part 1 **58**, SBBI04 (2019).
[11]M. Kim, S. J. Park, and H. Jin, J. Appl. Phys. **127**, 085105 (2020).
[12]T. K. H. Pham, M. Ribeiro, J. H. Park, N. J. Lee, K. H. Kang, E. Park, V. Q. Nguyen, A. Michel, C. S. Yoon, S. Cho, and T. H. Kim, Sci. Rep. **8**, 13907 (2018).
[13]Q. Zhang, S. Hikino, and S. Yunoki, Appl. Phys. Lett. **99**, 223303 (2011).
[14]L. Zhou, V. L. Grigoryan, S. Maekawa, X. Wang, and J. Xiao, Phys. Rev. B **91**, 045407 (2015).
[15]A. J. Caruana, M. D. Cropper, J. Zipfel, Z. Zhou, G. D. West, and K. Morrison, Phys. Rapid Res. Lett. **10**, 613–617 (2016).
[16]G.-P. Ojeda, M. Döbeli, and T. Lippert, Adv. Mater. Interfaces **5**, 1701062 (2018).
[17]A. Jacquot, B. Lenoir, M. O. Boffoué, and A. Dauscher, Appl. Phys. A **69**, S195–S199 (1999).
[18]J. E. Bateman, R. Dalgliesh, D. M. Duxbury, W. I. Helsby, S. A. Holt, C. J. Kinane, A. S. Marsh, N. J. Rhodes, E. M. Schooneveld, E. J. Spill, and R. Stephenson, Nucl. Instrum. Methods Phys. Res., Sect. A **698**, 168–176 (2013).
[19]P. A. Kienzle, B. B. Maranville, K. V. O'Donovan, J. F. Ankner, N. F. Berk, and C. F. Majkrzak, see https://www.nist.gov/ncnr/reflectometry-software 2017 for information about the Refl1d software.
[20]G. Awana, C. Cox, L. Stuffins, G. Venkat, K. Morrison, Z. Zhou, and D. Backes, Mater. Res. Express **7**, 106406 (2020).
[21]G. Venkat, C. D. W. Cox, A. Sola, V. Basso, and K. Morrison, Rev. Sci. Instrum. **91**, 073910 (2020).
[22]A. Sola, P. Bougiatioti, M. Kuepferling, D. Meier, G. Reiss, M. Pasquale, T. Kuschel, and V. Basso, Sci. Rep. **7**, 46752 (2017).
[23]E. van de Riet, C. J. Nillesen, and J. Dieleman, J. Appl. Phys. **74**, 2008 (1993).
[24]R. E. Leuchtner, J. S. Horwitz, and D. B. Chrisey, J. Appl. Phys. **83**, 5477 (1998).
[25]Y. Watanabe, M. Tanamura, S. Matsumoto, and Y. Seki, J. Appl. Phys. **78**, 2029–2036 (1995).

[26]M. Salim, T. Satoshi, A. Takao, N. Minoru, and H. Takanori, Q. J. Jpn. Weld. Soc. **21**, 338–343 (2003).
[27]G. Venkat, C. D. W. Cox, D. Voneshen, A. J. Caruana, A. Piovano, M. D. Cropper, and K. Morrison, Phys. Rev. Mater. **4**, 075402 (2020).
[28]R. Ramos, T. Kikkawa, K. Uchida, H. Adachi, I. Lucas, M. H. Aguirre, P. Algarabel, L. Morellón, S. Maekawa, E. Saitoh, and M. R. Ibarra, Appl. Phys. Lett. **102**, 072413 (2013).
[29]R. Bavontaweepanya, Y. Infahsaeng, E. Pongophas, W. Maiaugree, P. Piyasin, D. Palaporn, L. Wannasen, S. Pinitsoontorn, R. Pattanakul, H. Ramamoorthy, R. Somphonsane, P. Khayaiwong, and P. Wongjom, AIP Adv. **12**, 015320 (2022).
[30]A. Sola, V. Basso, M. Kuepferling, M. Pasquale, D. C. né Meier, G. Reiss, T. Kuschel, T. Kikkawa, K. Uchida, E. Saitoh, H. Jin, S. J. Watzman, S. Boona, J. Heremans, M. B. Jungflesich, W. Zhang, J. E. Pearson, A. Hoffmann, and H. W. Schumacher, IEEE Trans. Instrum. Meas. **68**, 1765–1773 (2019).
[31]M. Weiler, M. Althammer, M. Schreier, J. Lotze, M. Pernpeintner, S. Meyer, H. Huebl, R. Gross, A. Kamra, J. Xiao, Y.-T. Chen, H. J. Jiao, G. E. W. Bauer, and S. T. B. Goennenwein, Phys. Rev. Lett. **111**, 176601 (2013).
[32]X. Tao, Q. Liu, B. Miao, R. Yu, Z. Feng, L. Sun, B. You, J. Du, K. Chen, S. Zhang, L. Zhang, Z. Yuan, D. Wu, and H. Ding, Sci. Adv. **4**, eaat1670 (2018).
[33]F. D. Czeschka, L. Dreher, M. S. Brandt, M. Weiler, M. Althammer, I.-M. Imort, G. Reiss, A. Thomas, W. Schoch, W. Limmer, H. Huebl, R. Gross, and S. T. B. Goennenwein, Phys. Rev. Lett. **107**, 046601 (2011).
[34]K. Morrison, A. J. Caruana, G. Venkat, and C. D. W. Cox (2020). "ISIS Neutron and Muon Source Data Journal," PolRef. https://doi.org/10.5286/ISIS.E.RB2010586-1.
[35]G. Venkat, C. D. W. Cox, Z. Zhou, N. Leo, C. Kinane, A. J. Caruana, and K. Morrison (2023). "Enhancement of spin Seebeck effect in $Fe_3O_4$/Pt thin films with α-Fe nanodroplets - supporting data," Loughborough.